Topological superconducting phase in the vicinity of ferromagnetic phases

Yuan-Yuan Xiang,[1] Wan-Sheng Wang,[1] Qiang-Hua Wang,[1] and Dung-Hai Lee[2,3]

[1]*National Laboratory of Solid State Microstructures, Nanjing University, Nanjing 210093, China*
[2]*Department of Physics, University of California, Berkeley, Berkeley, California 94720, USA*
[3]*Materials Sciences Division, Lawrence Berkeley National Laboratory, Berkeley, California 94720, USA*

Through the study of concrete models we establish a strong tie between topological superconductivity and ferromagnetic spin correlations. Our result can be used as a guideline for the search for topological superconductors whose pairing symmetry is invariant under time reversal. The results are obtained by the functional renormalization group method.

I. INTRODUCTION

Topological insulators and superconductors have become a focus of interest in condensed-matter physics.[1,2] These states are characterized by symmetry-protected gapless boundary excitations. The existence of these excitations reflects the fact that it is impossible to smoothly connect a topological insulator/superconductor with its nontopological counterpart without crossing a quantum phase transition. Under the assumption of no electron-electron interaction, topological superconductors and insulators have been classified into ten symmetry classes.[3,4] In each spatial dimension precisely five of these classes have topological representatives. Examples of topological insulators include the time-reversal symmetry-breaking (T-breaking) integer quantum Hall insulator,[5] and the time-reversal-invariant (T-invariant) topological insulators in two[6] and three[7] dimensions. Examples of topological superfluids/superconductors include the T-breaking ^{3}He-A (Ref. 8) and Sr_2RuO_4,[9] and the T-invariant ^{3}He-B.[8]

In this fast-growing field, discovering new topological materials is clearly very important. While many topological insulators have been predicted and experimentally confirmed,[1,2,7] there is no conclusive evidence that topological superconductivity with time-reversal-invariant pairing symmetry is realized in any material. The recently discovered $Cu_xBi_2Se_3$ (Refs. 10–12) is an intriguing but not yet confirmed candidate. This makes the theoretical study of physical conditions that favor T-invariant topological superconductivity a pressing task.

Predicting topological superconductors is much harder than predicting topological insulators. This is because knowing the desired Bogoliubov–de Gennes (BdG) band structure[13] only meets half of the challenge. The other half requires knowledge of the microscopic interactions which favor the desired BdG band structure as the mean-field theory. Leaving topology aside, it is hard enough to predict superconductivity itself. This is because the energy scale involved in Cooper pairing is usually much smaller than the characteristic energies (e.g., the bandwidth) of the normal state. However, in the past five years various types of renormalization group methods have been used to compute the *effective interaction* responsible for the Cooper pairing in iron-based superconductors.[14,15] In this paper we apply a similar method to study topological superconductivity.

In the literature there are many interesting proposals for inducing topological superconductivity via the proximity effect.[16–19] (A notable exception is the intriguing proposal of

Ref. 12.) In these proposals, pairing is artificially induced by a (nontopological) superconductor. The reason the induced superconducting state is topological is due to the novel spin-orbit coupled electron wave functions in the normal state. The focus of this paper is on material which will be a topological superconductor by itself.

There are two classes (DIII and CI, according to Ref. 4) of T-invariant topological superconductor in three dimensions.[3,4] They are differentiated by the transformation properties with respect to time reversal and particle-hole conjugation. In this paper we focus on class DIII, for it has realization in space dimension $d = 1$, 2, and 3. We ask, "under what condition is T-invariant topological superconductivity favored?" We argue that it is when the ferromagnetic (to be precise, small wave vector magnetic) fluctuations are strong.

Due to practical limitations (on computation) we limit ourselves to two-dimensional (2D), i.e., thin-film, topological superconductors. Such systems inevitably break the spatial inversion symmetry because of the presence of the Rashba spin-orbit coupling term near the surface. As a result the superconductors under consideration are *noncentrosymmetric*. For this type of superconductor, parity-even and parity-odd pairing symmetries can mix. Many real superconducting materials are noncentrosymmetric. Examples include $CePt_3Si$,[20] $CeRhSi_3$,[21] $CeIrSi_3$,[22] and the superconductivity found at the interface of $LaAlO_3$ and $SrTiO_3$.[23] For discussions of topological pairing in centrosymmetric systems see, e.g., Ref. 24, and for noncentrosymmetric systems see, e.g., Ref. 25.

Using the functional renormalization group method, we establish a tie between topological superconductivity and ferromagnetic fluctuations. We provide different mechanisms that lead to strong ferromagnetic fluctuations and hence triplet pairing. Under such a condition, we show that a small Rashba coupling can induce T-invariant topological superconductivity. Our result implies that such a topological pairing is unlikely in superconducting materials where singlet pairing dominates. The paper concludes with a guideline and a few suggestions for systems that might realize T-invariant topological superconductivity.

The rest of this paper is structured as follows. In Sec. II we describe briefly the functional renormalization group method for our purpose, leaving the more technical details in the Appendix. In Secs. III and IV we provide two concrete models that lead to T-invariant topological superconductivity. In Sec. V we discuss the results and the relevance to experiments.
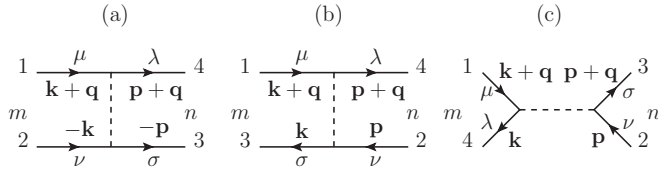
FIG. 1. A generic four-point vertex Γ_{1234} is rearranged into (a) P, (b) C, and (c) D channels. Here $\mathbf{k}, \mathbf{q}, \mathbf{p}$ are momenta; $\mu, \nu, \sigma, \lambda$ are spin indices; and m, n denote the form factors. On each side of the diagrams, the spin (and sublattice) labels are absorbed into the form-factor labels wherever applicable (see the main text).

II. METHOD

Technically this work requires us to generalize the functional renormalization group (FRG) approach[14,15,26,27] to Hamiltonians without spin rotation symmetry. In addition, because of the necessity to study small-momentum-transfer particle-hole scatterings we use a Matsubara frequency rather than a momentum cutoff. All calculations are carried out using the singular-mode functional renormalization group (SM-FRG) method.[27,28] More details on this method can be found in the Appendix.

Consider a generic fully antisymmetrized irreducible four-point vertex function Γ_{1234} in $\Psi_1^\dagger \Psi_2^\dagger (-\Gamma_{1234}) \Psi_3 \Psi_4$. Here 1,2,3,4 represent momentum and spin (and sublattice) indices. Figures 1(a)–1(c) are rearrangements of Γ_{1234} into the pairing (P), crossing (C), and direct (D) channels, each characterized by a collective momentum $\mathbf{q}$. In each channel the vertex function is decomposed as Eq. (A1) in the Appendix. There $\{f_m\}$ is a set of orthonormal lattice form factors.[29] The spin (and sublattice) indices are contained in the label of the form factors as shown in Figs. 1(a)–1(c). The decomposition in Eq. (A1) is exact if the form factors are complete, but a few of them are often enough to capture the leading instabilities.[27,28] The FRG flow equations for P, C, and D as a function of the cutoff scale Λ are given by Eqs. (A3)–(A5) in the Appendix. The effective interaction in the particle-particle (pp) and particle-hole (ph) channels are given, respectively, by $V_{pp} = -P/2$ and $V_{ph} = C$. [Because of antisymmetry D ($= -C$) does not yield any new information.] During the FRG flow we monitor the singular values of the matrix functions $V_{pp/ph}(\mathbf{q})$. The most negative singular values, $S_{pp/ph}$, occur at special momenta $\mathbf{q}_{pp/ph}$. While $\mathbf{q}_{pp}$ is usually zero, $\mathbf{q}_{ph}$ can evolve under RG flow before settling down to fixed values. The eigenfunction associated with S_{pp} is used to construct the gap function. Further details can be found in the Appendix.

III. TOPOLOGICAL PAIRING IN THE VICINITY OF VAN HOVE SINGULARITY

We consider spin-1/2 fermions hopping on a square lattice. The Hamiltonian is given by

$$H = \sum_{\mathbf{k}} \Psi_{\mathbf{k}}^\dagger [\epsilon(\mathbf{k})\sigma_0 + \lambda \vec{\gamma}(\mathbf{k}) \cdot \vec{\sigma}] \Psi_{\mathbf{k}} + U \sum_i n_{i\uparrow} n_{i\downarrow}. \quad (1)$$

Here $\Psi^\dagger = (\psi_\uparrow^\dagger, \psi_\downarrow^\dagger)$, $\epsilon(\mathbf{k}) = -2t(\cos k_x + \cos k_y) - 4t' \cos k_x \cos k_y - \mu$ is the normal state dispersion (t and t' are hopping amplitudes and μ is the chemical potential), i labels the lattice sites, and $n_{i\sigma} = \psi_{i\sigma}^\dagger \psi_{i\sigma}$. In addition, σ_0

is the 2×2 identity matrix and $\vec{\sigma}$ denotes the three Pauli matrices. In the Rashba spin-orbit coupling we consider $\vec{\gamma}(\mathbf{k}) = (-\sin k_y, \sin k_x, 0)$.

Combining the time-reversal and point-group (C_{4v} in the present case) symmetries, it can be shown that the Cooper pair operator $B^\dagger = \sum_{\mathbf{k}} \Psi_{\mathbf{k}}^\dagger \Delta_{\mathbf{k}} \Psi_{-\mathbf{k}}^{\dagger T}$ takes the form[30] $\Delta(\mathbf{k}) = [\phi(\mathbf{k})\sigma_0 + \vec{d}(\mathbf{k}) \cdot \vec{\sigma}]i\sigma_2$, where $\vec{d}(\mathbf{k})$ transforms, under the point group, like the product of $\phi(\mathbf{k})$ and $\vec{\gamma}(\mathbf{k})$. In the cases we have studied, to a good approximation, we can write

$$\Delta(\mathbf{k}) = [\phi(\mathbf{k})\sigma_0 + \chi(\mathbf{k})\hat{\gamma}(\mathbf{k}) \cdot \vec{\sigma}]i\sigma_2, \quad (2)$$

where $\hat{\gamma}(\mathbf{k}) = \vec{\gamma}(\mathbf{k})/|\vec{\gamma}(\mathbf{k})|$, and $\phi(\mathbf{k})$ and $\chi(\mathbf{k})$ are even functions of $\mathbf{k}$ and are real up to a global phase. They transform according to the same irreducible representation of the point group (for multidimensional representations there are several ϕ's and χ's). In Landau theory, ϕ and χ act as order parameters and can induce each other in the presence of the Rashba coupling ($\lambda \neq 0$).

It is important to note that the Rashba term splits each of the otherwise spin-degenerate Fermi surfaces into two. The spin-split Fermi surfaces are characterized by eigenvalues ± 1 of $\hat{\gamma}(\mathbf{k}) \cdot \vec{\sigma}$. In the case where $\phi(\mathbf{k})$ and $\chi(\mathbf{k})$ are nodeless, the gap function on the two split Fermi surfaces will have opposite sign if the magnitudes of $\chi(\mathbf{k})$ dominate over $\phi(\mathbf{k})$. It turns out that for *each pair* of Fermi pockets surrounding a T-invariant $\mathbf{k}$ point the above sign reversal leads to two counterpropagating Majorana edge modes. Thus, topological pairing requires the *triplet χ component* to be dominant. Moreover, sign reversal (in the gap function) on odd/even pairs of the spin-split Fermi surfaces (satisfying the condition specified above) will lead to strong/weak topological superconductivity.

For $t' = -0.475t$, $\mu = -2t$, and $\lambda = 0.01t$, the spin-split Fermi surfaces are shown in Fig. 2(a). They are pointy along $\hat{x}$ and $\hat{y}$, reflecting the existence of saddle points (van Hove
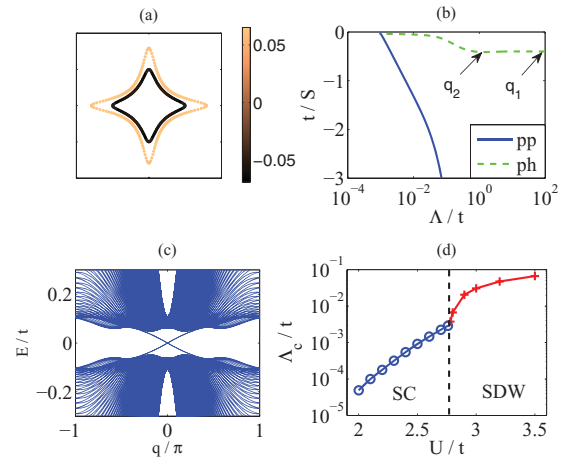

FIG. 2. (Color online) (a) The spin-split Fermi surfaces. The gray scale shows the values of the gap functions. The spin splitting is intentionally enlarged for a better view. (b) The SM-FRG flow of $S_{pp/ph}$ versus cutoff scale Λ. Arrows mark the evolution of the wave vector in the ph channel during the RG flow. (c) The low-energy BdG eigenspectrum in a strip (open along $\hat{x}$) as a function of the momentum $q\hat{y}$. (d) The phase diagram defined by the upper critical scale in the pp and ph channels as a function of U. The vertical dashed line marks the phase boundary.

singularities) on the Brillouin zone boundary. These features lead to enhanced ferromagnetic correlations via the Stoner mechanism. However, this mechanism overestimates the spin fluctuations by ignoring the overlaps to the other channels. The FRG method we apply here treats all channels on an equal footing and provides a mechanism of triplet pairing due to enhanced ferromagnetic fluctuations. The form factors used in our SM-FRG extend up to second neighbors in real space.[29] The RG flow of $S_{pp/ph}$ is shown in Fig. 2(b) for $U = 2.5t$. The arrows associated with the S_{ph} flow record the $\mathbf{q}_{ph}$ evolution from $\mathbf{q}_1 = (\pi,\pi)$ to $\mathbf{q}_2 = 0$. By inspecting the spin structure of the $\mathbf{q}_2$ singular mode we find it corresponds to ferromagnetic fluctuation. The increased ferromagnetic fluctuation around $\mathbf{q}_2$ enhances pairing in the triplet channel via their mutual overlaps (see the Appendix). The gap function is determined by the singular mode associated with S_{pp} at the diverging cutoff scale. The result is a dominant χ component together with a much smaller ϕ component. The corresponding gap function on the two Fermi surfaces is shown in Fig. 2(a) (grayscale). A sign change is clearly visible. According to the established criterion,[2] this pairing state is topological. To verify this, we calculate the BdG energy spectrum using the obtained pairing form factor in a strip geometry (open boundary along $\hat{x}$). The resulting eigenenergies as a function of $q = k_y$ are shown in Fig. 2(c). There are two in-gap counterpropagating Majorana edge modes associated with each edge.

Had we turned off the Rashba coupling, the leading pairing channel (p wave) would be two-fold degenerate (with dominant amplitudes on first-neighbor bonds). Under this condition even an infinitesimal Rashba coupling breaks the degeneracy by linearly recombining the p waves into $\Delta(\mathbf{k}) = i \sin k_x \sigma_0 + \sin k_y \sigma_3$, or $\chi(\mathbf{k}) = |\vec{\gamma}(\mathbf{k})|$ in Eq. (2), leading to a gap function $\pm \chi(\mathbf{k})$ on the infinitesimally split Fermi surfaces. Interestingly this gap function has the same symmetry as the two-dimensional version of the ^{3}He-B phase. In addition, the Rashba coupling plays a similar role as the parity-invariant spin-orbit interaction in ^{3}He: they both lift the degeneracy in the pairing channel.

Figure 2(d) is a phase diagram of the present model, defined by the upper critical scale in the pp and ph channels. With t' and μ fixed, we find that for $U < 2.77t$ the system is in the topological triplet superconducting state, while the ferromagnetic spin-density-wave (SDW) state is realized for $U > 2.77t$.

IV. TOPOLOGICAL PAIRING ENHANCED BY INTERPOCKET SCATTERING

In this section we show another route to topological pairing. In this case pairing is triggered by inter-Fermi surface scattering in a way similar to the pairing in the pnictides.[14,15]

Consider a honeycomb lattice. The single-particle Hamiltonian is given by

$$H_0 = -\sum_{i\delta} \Psi_i^\dagger t_\delta \Psi_{i+\delta} - i\lambda \sum_{i\delta_{nn}} \Psi_i^\dagger (\hat{z} \times \vec{\delta}_{nn} \cdot \vec{\sigma}) \Psi_{i+\delta_{nn}}$$
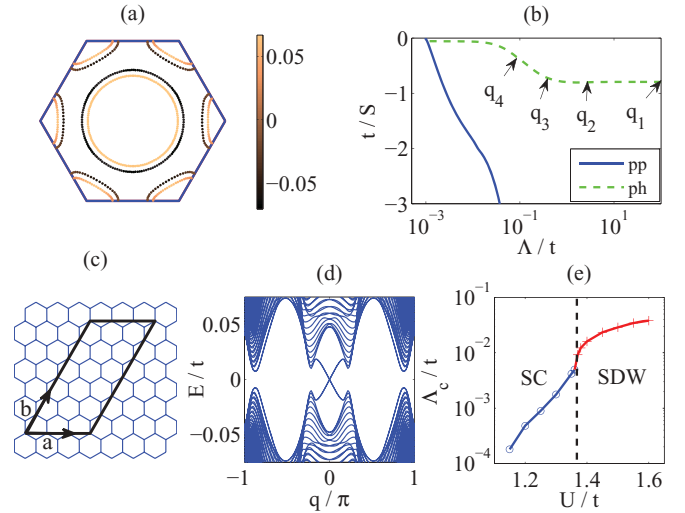$$- \mu \sum_i \Psi_i^\dagger \Psi_i. \tag{3}$$

FIG. 3. (Color online) (a) The Fermi pockets and the associated gap functions (gray scale, in units of t). The spin splitting between each pair of Fermi pockets is enlarged for clarity. The hexagon is the zone boundary. (b) The SM-FRG flow of $S_{pp/ph}$ versus the cutoff scale Λ. Arrows mark sharp changes of $\mathbf{q}_{ph}$ during the RG flow. (c) A strip (marked by the thick lines) open along $\mathbf{a}$ and periodic along $\mathbf{b}$ directions ($\mathbf{a}$ and $\mathbf{b}$ are parallel to the primitive lattice vectors). (d) The low-energy BdG eigenspectrum for (c) as a function of the conserved momentum q along $\mathbf{b}$. (e) The phase diagram defined by the upper critical scale in the pp and ph channels as a function of U. The vertical dashed line marks the phase boundary.

Here i labels lattice sites, δ runs over the first- and second-neighbor bonds, with $t_\delta = t, t'$. The spin-dependent hopping, the Rashba term, is limited to the nearest-neighbor bonds δ_{nn}. Choosing a lattice site as the origin, the point group is C_{3v}. For the SM-FRG calculation, we choose the form factors up to the second neighbors.[29] (Since the honeycomb lattice has two sites per unit cell the labels of the form factors in Fig. 1 include the sublattice indices.[27]) The Fermi surfaces for $t' = 0.357t$, $\lambda = 0.02t$, and $\mu = 1.664t$ are shown in Fig. 3(a). There are a few interesting features of the band structure that are worth noting: (1) The Fermi surfaces encircle either the zone center (Γ) or the zone corners (K and K'). However, only Γ is T-invariant, hence according to Ref. 2 only the Γ Fermi surfaces are topologically relevant. (2) The Γ and K pockets have nearby segments and hence allow small-momentum-transfer particle-hole scattering. If such scattering is magnetic, it corresponds to nearly ferromagnetic fluctuations and hence can induce triplet and topological pairing.

In the following we show for $U = 1.26t$ this is exactly what happens. During the RG flow shown in Fig. 3(b), the strength of S_{ph} increases and $\mathbf{q}_{ph}$ evolves from $\mathbf{q}_1 = (0.667,1.152)\pi$ to $\mathbf{q}_2 = 0$, $\mathbf{q}_3 = (0.250,0.048)\pi$, and finally settles down at $\mathbf{q}_4 = (0.333,0.192)\pi$. We have checked that $\mathbf{q}_4$ corresponds to the scattering between nearby parallel segments between the Γ and K pockets. Inspection of the spin structure of the singular mode associated with $\mathbf{q}_{2,3,4}$ reveals that it corresponds to spin fluctuations. As such fluctuations are enhanced, they cause S_{pp} to grow in magnitude and eventually diverge at a relatively high critical scale. The resulting gap function is shown in Fig. 3(a) in grayscale. It is *fully gapped on all Fermi surfaces* and has

opposite sign on each pair of spin-split pockets. Since the K pockets are topologically irrelevant, the sign change between the Γ Fermi surfaces implies the pairing is strong-topological. To verify this we consider a strip schematically shown in Fig. 3(c). It is open along **a** and periodic along **b** directions. The BdG energy spectrum as a function of the momentum $q = \mathbf{k} \cdot \hat{b}$ is shown in Fig. 3(d). There are two branches of Majorana modes at each edge. Figure 3(e) is a phase diagram for the present model with fixed μ. The topological superconducting phase is realized for $U < 1.365t$, while ferromagneticlike SDW instability is realized for $U > 1.365t$.

V. DISCUSSION

Thus in both of the above examples we have seen

small momentum magnetic fluctuations

$\Rightarrow$ degenerate triplet pairing, and

degenerate triplet pairing + Rashba coupling

$\Rightarrow$ topological pairing.

We notice that in each case there is a finite range in the parameter space where topological pairing is realized. The fact that ferromagnetic fluctuations enhance triplet pairing has a long history. These include the works on the pairing of ^{3}He,[8,31,32] and the extension of the Kohn-Luttinger theorem to p-wave pairing for 2D and three-dimensional (3D) electron gas in the dilute limit.[33,34] Examples of works on lattice systems include Refs. 35–37.

It is important to emphasize that if pairing is predominantly singlet a weak Rashba coupling can only induce a small triplet component and hence is insufficient to induce the desired sign change in the gap function. Of course this does not rule out the possibility of topological pairing in the presence of strong spin-orbit interaction.

Many noncentrosymmetric superconductors appear near the antiferromagnetic rather than the ferromagnetic phase. These include CePt$_3$Si, CeRhSi$_3$, CeIrSi$_3$, and CeCoGe$_3$. For these materials topological superconductivity is unlikely. There are also many materials where superconductivity appears near ferromagnetism. Examples include Li$_2$Pd$_3$B, Li$_2$Pt$_3$B, URhGe, HoMo$_6$Se$_8$, ErRh$_4$B$_4$,[38] iron under pressure,[39] and the interface superconductivity of LaAlO$_3$/SrTiO$_3$.[23] In these systems it should be more likely to find topological pairing.

In conclusion, our functional renormalization group investigations indicate that T-invariant topological superconductivity in symmetry class DIII should occur in systems close to the ferromagnetic (or small-wave-vector magnetic) instability. Band-structure-wise, in the absence of Rashba coupling, these systems should have an odd number of spin-degenerate Fermi pockets (each enclosing a T-invariant momentum) in order for strong topological pairing to occur.

ACKNOWLEDGMENTS

APPENDIX

Here we provide the technical details of the SM-FRG method.[27,28] We begin by reviewing the definition of the vertex functions used in the main text. Consider a generic fully antisymmetrized irreducible four-point vertex function Γ_{1234} in $\Psi_1^\dagger \Psi_2^\dagger (-\Gamma_{1234})\Psi_3 \Psi_4$. Here 1,2,3,4 represent momentum and spin (and sublattice) indices. Figures 4(a)–4(c) are rearrangements of Γ_{1234} into the pairing (P), crossing (C), and direct (D) channels, each characterized by a collective momentum **q**. The rest momentum dependence of the vertex function can be decomposed as

$$\Gamma^{\mu\nu\sigma\lambda}_{\mathbf{k+q},-\mathbf{k},-\mathbf{p},\mathbf{p+q}} \rightarrow \sum_{mn} f_m^*(\mathbf{k}) P_{mn}(\mathbf{q}) f_n(\mathbf{p}),$$

$$\Gamma^{\mu\nu\sigma\lambda}_{\mathbf{k+q},\mathbf{p},\mathbf{k},\mathbf{p+q}} \rightarrow \sum_{mn} f_m^*(\mathbf{k}) C_{mn}(\mathbf{q}) f_n(\mathbf{p}), \qquad \text{(A1)}$$

$$\Gamma^{\mu\nu\sigma\lambda}_{\mathbf{k+q},\mathbf{p},\mathbf{p+q},\mathbf{k}} \rightarrow \sum_{mn} f_m^*(\mathbf{k}) D_{mn}(\mathbf{q}) f_n(\mathbf{p}).$$

Here $\{f_m\}$ is a set of orthonormal lattice form factors. The spin (and sublattice) indices are contained in the label of the form factors as shown in Figs. 4(a)–4(c). The decomposition in Eq. (A1) is exact if the form factors are complete, but in practice a few of them are often enough to capture the leading instabilities.[27,28] Because of full antisymmetry, the matrices C and D satisfy $D = -C$ and are therefore not independent. In the following, D is used for bookkeeping purposes.

Ignoring the spin and sublattice labels for the moment, the form factors are given by

$$f_m(\mathbf{k}) = \sum_{\mathbf{r}} f_m(\mathbf{r}) \exp(-i\mathbf{k} \cdot \mathbf{r}), \qquad \text{(A2)}$$

where $f_m(\mathbf{r})$ transforms according to an irreducible representation of the point group, and **r** are the bond vectors connecting the two Ψ's (or two $\Psi^\dagger$'s) in Fig. 4(a) and one Ψ and one $\Psi^\dagger$ in Figs. 4(b) and 4(c). In our calculation we choose form factors up to the second-neighbor bonds. We have checked
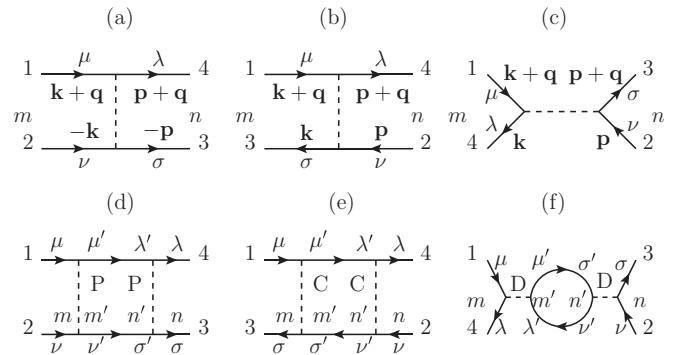
FIG. 4. A generic 4-point vertex Γ_{1234} is rearranged into P-, C-, and D-channels in (a)–(c), respectively. Here $\mathbf{k}, \mathbf{q}, \mathbf{p}$ are momenta, $\mu, \nu, \sigma, \lambda$ denote spins, and m, n denote the form factors. On each side of the diagrams, the spin (and sublattice) labels are absorbed into the form factor labels wherever applicable. The one-loop diagrams that contribute to ∂P, ∂C and ∂D are shown in (d)–(f), respectively.

that longer-range form factors do not change the results qualitatively. To be specific, for a square lattice, the real-space form factors we used are (1) $f_1 = 1$ for on-site; (2) $f_2 = 1/2$, $f_3 = (1/2)\cos 2\theta_{\mathbf{r}}$, $f_4 = \sqrt{1/2}\cos\theta_{\mathbf{r}}$, and $f_5 = \sqrt{1/2}\sin\theta_{\mathbf{r}}$ for first neighbors, where $\theta_{\mathbf{r}}$ is the azimuthal angle of $\mathbf{r}$; and (3) $f_6 = 1/2$, $f_7 = (1/2)\sin 2\theta_{\mathbf{r}}$, $f_8 = \sqrt{1/2}\cos(\theta_{\mathbf{r}} - \pi/4)$, and $f_9 = \sqrt{1/2}\sin(\theta_{\mathbf{r}} - \pi/4)$ for second neighbors. For hexagonal lattices, the form factors we used are (1) $f_1 = 1$ for on-site; (2) $f_2 = \sqrt{1/3}$, $f_3 = \sqrt{2/3}\cos\theta_{\mathbf{r}}$, and $f_4 = \sqrt{2/3}\sin\theta_{\mathbf{r}}$ for first neighbors; and (3) $f_5 = \sqrt{1/6}$, $f_6 = \sqrt{1/3}\cos\theta_{\mathbf{r}}$, $f_7 = \sqrt{1/3}\sin\theta_{\mathbf{r}}$, $f_8 = \sqrt{1/3}\cos 2\theta_{\mathbf{r}}$, $f_9 = \sqrt{1/3}\sin 2\theta_{\mathbf{r}}$, and $f_{10} = \sqrt{1/6}\cos 3\theta_{\mathbf{r}}$ for second neighbors. Notice that the first-neighbor bonds stem from different sublattices and are negative to each other.

In the case where sublattices are involved, the form factor label m also includes the sublattice indices associated with the two Ψ's (or $\Psi^\dagger$'s), or the Ψ and $\Psi^\dagger$. However, once $\mathbf{r}$ is fixed only one of these sublattice indices is independent. We include the independent sublattice index in the form factor label, $(m,a) \to m$. Here a labels, e.g., the fermion field 1 or 4 in Fig. 4(a), 1 or 4 in Fig. 4(b), and 1 or 3 in Fig. 4(c). The sublattice index is an independent label because point-group operations do not mix sublattices when the origin is chosen to be a lattice site.

The total number of form factors, N, in a calculation is determined by the number of real space neighbors, the number of sublattices, and the four spin combinations $(\mu,\nu) = \uparrow\uparrow, \uparrow\downarrow, \downarrow\uparrow, \downarrow\downarrow$ associated with two Ψ (P channel) or the Ψ and $\Psi^\dagger$ (C and D channels). Thus P, C, and D are all $N \times N$ matrix functions of momentum $\mathbf{q}$.

The Feynman diagrams associated with one-loop contributions to the flow of the irreducible four-point vertex function are given in Figs. 4(d)–4(f). They represent the partial changes ∂P, ∂C, and ∂D, respectively. [Notice that the three diagrams in Figs. 4(d)–4(f) become the usual five diagrams in the spin-conserved case.] The internal Green's functions are convoluted with the form factors hence in matrix form,

$$\partial P/\partial\Lambda = P\chi'_{\mathrm{pp}}P/2,$$
$$\partial C/\partial\Lambda = C\chi'_{\mathrm{ph}}C, \qquad\qquad (A3)$$
$$\partial D/\partial\Lambda = -D\chi'_{\mathrm{ph}}D,$$

where we have suppressed the dependence of the collective momentum $\mathbf{q}$, and

$$
\begin{aligned}
(\chi'_{\mathrm{pp}})_{mn} &= \frac{\partial}{\partial\Lambda} \int \frac{d\omega_n}{2\pi} \int \frac{d^2\mathbf{p}}{S_{\mathrm{BZ}}} f_m(\mathbf{p}) G(\mathbf{p}+\mathbf{q}, i\omega_n) G(-\mathbf{p}, -i\omega_n) f_n^*(\mathbf{p}) \theta(|\omega_n| - \Lambda) \\
&= -\frac{1}{2\pi} \int \frac{d^2\mathbf{p}}{S_{\mathrm{BZ}}} f_m(\mathbf{p}) G(\mathbf{p}+\mathbf{q}, i\Lambda) G(-\mathbf{p}, -i\Lambda) f_n^*(\mathbf{p}) + (\Lambda \to -\Lambda), \\
(\chi'_{\mathrm{ph}})_{mn} &= \frac{\partial}{\partial\Lambda} \int \frac{d\omega_n}{2\pi} \int \frac{d^2\mathbf{p}}{S_{\mathrm{BZ}}} f_m(\mathbf{p}) G(\mathbf{p}+\mathbf{q}, i\omega_n) G(\mathbf{p}, i\omega_n) f_n^*(\mathbf{p}) \theta(|\omega_n| - \Lambda) \\
&= -\frac{1}{2\pi} \int \frac{d^2\mathbf{p}}{S_{\mathrm{BZ}}} f_m(\mathbf{p}) G(\mathbf{p}+\mathbf{q}, i\Lambda) G(\mathbf{p}, i\Lambda) f_n^*(\mathbf{p}) + (\Lambda \to -\Lambda),
\end{aligned}
\qquad (A4)
$$

where G is the free fermion Green's function, and S_{BZ} is the total area of the Brillouin zone. Here $\Lambda > 0$ is the infrared cutoff of the Matsubara frequency ω_n. As in usual FRG implementation, the self-energy correction and frequency dependence of the vertex function are ignored.

Since ∂P, ∂C, and ∂D come from independent one-loop diagrams, they contribute independently to the full $d\Gamma_{1234}$, which needs to be projected onto the three channels. Therefore, the full flow equations are given by, formally,

$$
\begin{aligned}
dP/d\Lambda &= \partial P/\partial\Lambda + \hat{P}(\partial C/\partial\Lambda + \partial D/\partial\Lambda), \\
dC/d\Lambda &= \partial C/\partial\Lambda + \hat{C}(\partial P/\partial\Lambda + \partial D/\partial\Lambda), \qquad (A5) \\
dD/d\Lambda &= \partial D/\partial\Lambda + \hat{D}(\partial P/\partial\Lambda + \partial C/\partial\Lambda),
\end{aligned}
$$

where $\hat{P}$, $\hat{C}$, and $\hat{D}$ are the projection operators in the sense of Eq. (A1). Here we have used the fact that $\hat{K}(\partial K) = \partial K$ for $K = P, C, D$. In Eq. (A5) the terms preceded by the projection operators represent the overlaps of different channels. For two channels to overlap, the spatial coordinates of all four fermion fields must lie within the range set of the form factors. In the actual calculation the projections in Eq. (A5) are performed in real space.

The effective interaction in the particle-particle (pp) and particle-hole (ph) channels are given, respectively, by $V_{\mathrm{pp}} = -P/2$ and $V_{\mathrm{ph}} = C$. By singular value decomposition, we determine the leading instability in each channel,

$$V_X^{mn}(\mathbf{q}_X) = \sum_\alpha S_X^\alpha \phi_X^\alpha(m) \psi_X^\alpha(n), \qquad (A6)$$

where $X = \mathrm{pp}, \mathrm{ph}$; S_X^α is the singular value of the αth singular mode; and ϕ_X^α and ψ_X^α are the right and left eigenvectors of V_X, respectively. We fix the phase of the eigenvectors by requiring $\mathrm{Re}[\sum_m \phi_X^\alpha(m)\psi_X^\alpha(m)] > 0$ so that $S_X^\alpha < 0$ corresponds to an attractive mode in the X channel.

In the pp channel $\mathbf{q}_{\mathrm{pp}} = 0$ corresponds to the zero center-of-mass momentum Cooper instability. The matrix gap function $\Delta_{\mathbf{k}}$ in the spin and sublattice basis is determined as follows. A singular mode $\phi_{\mathrm{pp}}^\alpha$ leads to a pair operator (in the momentum space),

$$\Psi_{\mathbf{k}}^\dagger \Delta_{\mathbf{k}} \Psi_{-\mathbf{k}}^{\dagger T} = \sum_{m=(m,a,\mu,\nu)} \psi_{a\mu}^\dagger(\mathbf{k}) \phi_{\mathrm{pp}}^\alpha(m) f_m(\mathbf{k})^* \psi_{a_m\nu}^\dagger(-\mathbf{k}). \quad (A7)$$

Here a is the independent sublattice index, a_m is the second sublattice index determined by a and m as discussed earlier,

and μ,ν are spin indices. The parity of $\Delta_{\mathbf{k}}$ under space inversion determines the singlet and triplet components. The gap function in the band eigenbasis can be determined by the unitary transformation

$$\tilde{\Psi}_{\mathbf{k}}^{\dagger} = \Psi_{\mathbf{k}}^{\dagger} U_{\mathbf{k}}^{\dagger}, \tag{A8}$$

where the columns of $U_{\mathbf{k}}^{\dagger}$ are the Bloch states $\{|\mathbf{k},n\rangle\}$ (n is the band index). Under Eq. (A8) the pairing matrix transforms into

$$\tilde{\Delta}_{\mathbf{k}} = U_{\mathbf{k}} \Delta_{\mathbf{k}} U_{-\mathbf{k}}^{T}. \tag{A9}$$

In the weak-coupling case (i.e., when the magnitude of the superconducting gap is much smaller than the bandwidth), only the diagonal part of $\tilde{\Delta}$ (i.e., intra-Fermi surface pairing) is important. Since Eq. (A9) involves Bloch states at two different momenta, the phases of the associated Bloch states enter $\tilde{\Delta}$. Since there is time-reversal symmetry we fix the Bloch-state phase at $\mathbf{k}$ and $-\mathbf{k}$ by demanding $\hat{T}|\mathbf{k},n\rangle = |-\mathbf{k},n\rangle$ and $\hat{T}^2|\mathbf{k},n\rangle = -|\mathbf{k},n\rangle$, where $\hat{T} = i\sigma_2 K$ is the time-reversal operator.

In the particle-hole channel, we calculate the singular values associated with $V_{\text{ph}}(\mathbf{q})$ at all momenta $\mathbf{q}$. Unlike the Cooper channel, the most negative singular value can occur at nonzero momentum $\mathbf{q}_{\text{ph}}$. The associated particle-hole operator is given by

$$\Psi_{\mathbf{k}+\mathbf{q}}^{\dagger} \Pi_{\mathbf{k}} \Psi_{\mathbf{k}} = \sum_{m=(m,a,\mu,\nu)} \psi_{a\mu}^{\dagger}(\mathbf{k}+\mathbf{q}) \phi_{\text{ph}}^{\alpha}(m) f_m^*(\mathbf{k}) \psi_{a_m\nu}(\mathbf{k}). \tag{A10}$$

Usually the on-site form factor dominates in the particle-hole channel. By inspecting the spin structure of the on-site form factor one can easily determine whether the instability is chargelike or spinlike.

[1] For a review see M. Z. Hasan and C. L. Kane, Rev. Mod. Phys. **82**, 3045 (2010).

[2] For a review see X.-L. Qi and S.-C. Zhang, Rev. Mod. Phys. **83**, 1057 (2011).

[3] A. Y. Kitaev, AIP Conf. Proc. **1134**, 22 (2009).

[4] A. P. Schnyder, S. Ryu, A. Furusaki, and A. W. W. Ludwig, Phys. Rev. B **78**, 195125 (2008); AIP Conf. Proc. **1134**, 10 (2009); S. Ryu, A. P. Schnyder, A. Furusaki, and A. W. W. Ludwig, New J. Phys. **12**, 065010 (2010).

[5] K. von Klitzing, G. Dorda, and M. Pepper, Phys. Rev. Lett. **45**, 494 (1980); D. J. Thouless, M. Kohmoto, M. P. Nightingale, and M. den Nijs, *ibid.* **49**, 405 (1982).

[6] M. König, S. Wiedmann, C. Brüne, A. Roth, H. Buhmann, L. W. Molenkamp, X.-L. Qi, and S.-C. Zhang, Science **318**, 766 (2007).

[7] D. Hsieh, D. Qian, L. Wray, Y. Xia, Y. S. Hor, R. J. Cava, and M. Z. Hasan, Nature (London) **452**, 970 (2008); D. Hsieh, Y. Xia, D. Qian, L. Wray, J. H. Dil, F. Meier, J. Osterwalder, L. Patthey, J. G. Checkelsky, N. P. Ong, A. V. Fedorov, H. Lin, A. Bansil, D. Grauer, Y. S. Hor, R. J. Cava, and M. Z. Hasan, *ibid.* **460**, 1101 (2009); D. Hsieh, Y. Xia, D. Qian, L. Wray, F. Meier, J. H. Dil, J. Osterwalder, L. Patthey, A. V. Fedorov, H. Lin, A. Bansil, D. Grauer, Y. S. Hor, R. J. Cava, and M. Z. Hasan, Phys. Rev. Lett. **103**, 146401 (2009); D. Hsieh, Y. Xia, L. Wray, D. Qian, A. Pal, J. H. Dil, J. Osterwalder, F. Meier, G. Bihlmayer, C. L. Kane, Y. S. Hor, R. J. Cava, and M. Z. Hasan, Science **323**, 919 (2009); Y. Xia, D. Qian, D. Hsieh, L. Wray, A. Pal, H. Lin, A. Bansil, D. Grauer, Y. S. Hor, R. J. Cava, and M. Z. Hasan, Nat. Phys. **5**, 398 (2009); Y. L. Chen, J. G. Analytis, J.-H. Chu, Z. K. Liu, S.-K. Mo, X. L. Qi, H. J. Zhang, D. H. Lu, X. Dai, Z. Fang, S. C. Zhang, I. R. Fisher, Z. Hussain, and Z.-X. Shen, Science **325**, 178 (2009).

[8] For a review see D. Vollhardt, and P. Wölfle, *The Superfluid Phases of Helium* (Taylor and Francis, Philadelphia, 1990).

[9] For a review and references see A. P. Mackenzie and Y. Maeno, Rev. Mod. Phys. **75**, 657 (2003).

[10] Y. S. Hor, A. J. Williams, J. G. Checkelsky, P. Roushan, J. Seo, Q. Xu, H. W. Zandbergen, A. Yazdani, N. P. Ong, and R. J. Cava, Phys. Rev. Lett. **104**, 057001 (2010).

[11] S. Sasaki, M. Kriener, K. Segawa, K. Yada, Y. Tanaka, M. Sato, and Y. Ando, Phys. Rev. Lett. **107**, 217001 (2011).

[12] Liang Fu and E. Berg, Phys. Rev. Lett. **105**, 097001 (2010).

[13] A. P. Schnyder and S. Ryu, Phys. Rev. B **84**, 060504 (2011).

[14] F. Wang, H. Zhai, Y. Ran, A. Vishwanath, and D.-H. Lee, Phys. Rev. Lett. **102**, 047005 (2009); A. V. Chubukov, D. V. Efremov, and I. Eremin, Phys. Rev. B **78**, 134512 (2008); R. Thomale, C. Platt, J. P. Hu, C. Honerkamp, and B. A. Bernevig, *ibid.* **80**, 180505 (2009); H. Zhai, F. Wang, and D.-H. Lee, *ibid.* **80**, 064517 (2009).

[15] For a review see Fa Wang and D.-H. Lee, Science **332**, 200 (2011).

[16] Liang Fu, C. L. Kane, and E. J. Mele, Phys. Rev. Lett. **98**, 106803 (2007); Liang Fu and C. L. Kane, *ibid.* **100**, 096407 (2008).

[17] M. Sato, Y. Takahashi, and S. Fujimoto, Phys. Rev. Lett. **103**, 020401 (2009); J. D. Sau, R. M. Lutchyn, S. Tewari, and S. Das Sarma, *ibid.* **104**, 040502 (2010).

[18] J. Alicea, Phys. Rev. B **81**, 125318 (2010).

[19] J. Linder, Y. Tanaka, T. Yokoyama, A. Sudbø, and N. Nagaosa, Phys. Rev. Lett. **104**, 067001 (2010); Phys. Rev. B **81**, 184525 (2010).

[20] E. Bauer, G. Hilscher, H. Michor, Ch. Paul, E. W. Scheidt, A. Gribanov, Yu. Seropegin, H. Nöel, M. Sigrist, and P. Rogl, Phys. Rev. Lett. **92**, 027003 (2004).

[21] N. Kimura, K. Ito, K. Saitoh, Y. Umeda, H. Aoki, and T. Terashima, Phys. Rev. Lett. **95**, 247004 (2005).

[22] I. Sugitani, Y. Okuda, H. Shishido, T. Yamada, A. Thamizhavel, E. Yamamoto, T. D. Matsuda, Y. Haga, T. Takeuchi, R. Settai, and Y. ōnuki, J. Phys. Soc. Jpn. **75**, 043703 (2006).

[23] N. Reyren, S. Thiel, A. D. Caviglia, L. F. Kourkoutis, G. Hammerl, C. Richter, C. W. Schneider, T. Kopp, A.-S. Rüetschi, D. Jaccard, M. Gabay, D. A. Muller, J.-M. Triscone, and J. Mannhart, Science **317**, 1196 (2007).

[24] G. E. Volovik and L. P. Gorkov, Sov. Phys. JETP **61**, 843 (1985).

[25] M. Sato and S. Fujimoto, Phys. Rev. B **79**, 094504 (2009); M. Sato, Y. Takahashi, and S. Fujimoto, *ibid.* **82**, 134521 (2010); P. Ghosh, J. D. Sau, S. Tewari, and S. Das Sarma, *ibid.* **82**, 184525 (2010); C. K. Lu and S. Yip, *ibid.* **78**, 132502 (2008).

[26] C. Honerkamp, M. Salmhofer, N. Furukawa, and T. M. Rice, Phys. Rev. B **63**, 035109 (2001).

[27] Wan-Sheng Wang, Yuan-Yuan Xiang, Qiang-Hua Wang, Fa Wang, Fan Yang, and Dung-Hai Lee, Phys. Rev. B **85**, 035414 (2012).

[28] C. Husemann and M. Salmhofer, Phys. Rev. B **79**, 195125 (2009).

[29] In real space (ignoring other labels), the form factors $\{f_m(\mathbf{r})\}$ are irreducible representations of the point group, where $\mathbf{r}$ is the bond vector connecting lattice sites. Bond vectors connected by point-group operations form a support for the form factor. For a given support, the number of independent form factors equals the number of independent bonds therein.

[30] For a review and references see M. Sigrist, *Lectures on the Physics of Strongly Correlated Systems XIII*, edited by A. Avella and F. Mancini (American Institute of Physics, Melville, NY, 2009).

[31] A. Layzer and D. Fay, Int. J. Magn. **1**, 135 (1971).

[32] P. W. Anderson and W. F. Brinkman, *The Helium Liquids*, edited by J. G. M. Armitage and I. E. Farquhar (Academic, New York, 1975), pp. 315-416; P. W. Anderson, Phys. Rev. B **30**, 1549 (1984).

[33] D. Fay and A. Layzer, Phys. Rev. Lett. **20**, 187 (1968).

[34] M. Yu. Kagan and A. V. Chubukov, Pisma Zh. Eksp. Teor. Fiz. **47**, 525 (1988); A. V. Chubukov, Phys. Rev. B **48**, 1097 (1993).

[35] A. V. Chubukov and J. P. Lu, Phys. Rev. B **46**, 11163 (1992).

[36] C. Honerkamp and M. Salmhofer, Physica C **408-410**, 302 (2004).

[37] Y. Hori and A. Goto, J. Phys., Conf. Ser. **150**, 052072 (2009); S. Onari, R. Arita, K. Kuroki, and H. Aoki, Phys. Rev. B **70**, 094523 (2004); Z. Szabo and Z. Gulacsi, Philos. Mag. B **76:5**, 833 (1997).

[38] Dai Aoki and Jacques Flouquet, J. Phys. Soc. Jpn. **81**, 011003 (2012).

[39] Katsuya Shimizu *et al.*, Nature (London) **412**, 316 (2001).